Research Article
Vol. 26, No. 22 | 29 Oct 2018 | OPTICS EXPRESS 28604
Optics EXPRESS

Using a passively stable attosecond beamline for relative phjavascript:void(0);otoemission time delays at high XUV photon energies

AROHI JAIN,[1] THOMAS GAUMNITZ,[1,*] ANATOLI KHEIFETS,[2] AND HANS JAKOB WÖRNER[1]

[1] *Laboratorium für Physikalische Chemie, ETH Zürich,Vladimir-Prelog-Weg 2, 8093 Zürich, Switzerland*
[2] *Research School of Physics and Engineering, The Australian National University, Canberra ACT 2601, Australia*
[*] *Thomas.Gaumnitz@phys.chem.ethz.ch*

Abstract: We present and demonstrate an experimental scheme that enables overlap-free reconstruction of attosecond beating by the interference of two-photon transition (RABBITT) measurements at high extreme-ultraviolet (XUV) photon energies. A compact passively-stabilized attosecond beamline employing a multilayer (ML) mirror allows us to obtain XUV pulses consisting of only two odd high-harmonic orders from an attosecond pulse train (APT). We compare our new technique to existing schemes that are used to perform RABBITT measurements and discuss how our scheme resolves the limitations imposed by spectral complexity of the harmonic comb at high photon energies. We further demonstrate first applications of our scheme for rare gases and gas mixtures, and show that this scheme can be extended to gas-molecule mixtures.

OCIS codes: (020.0020) Atomic and molecular physics; (320.7100) Ultrafast measurements; (260.5210) Photoionization; (140.7240) UV, EUV, and X-ray lasers.

References and links

1. P. B. Corkum and F. Krausz, “Attosecond science,” Nat. Phys. **3**, 381–387 (2007).
2. E. Goulielmakis, Z.-H. Loh, A. Wirth, R. Santra, N. Rohringer, V. S. Yakovlev, S. Zherebtsov, T. Pfeifer, A. M. Azzeer, M. F. Kling, S. R. Leone, and F. Krausz, “Real-time observation of valence electron motion,” Nature. **466**, 739–743 (2010).
3. V. Gruson, L. Barreau, Á. Jiménez-Galan, F. Risoud, J. Caillat, A. Maquet, B. Carré, F. Lepetit, J.-F. Hergott, T. Ruchon, L. Argenti, R. Taïeb, F. Martín, and P. Salières, “Attosecond dynamics through a Fano resonance: Monitoring the birth of a photoelectron,” Science. **354**, 734–738 (2016).
4. F. Krausz and M. Ivanov, “Attosecond physics,” Rev. Mod. Phys. **81**, 163 (2009).
5. A. Kaldun, A. Blättermann, V. Stooß, S. Donsa, H. Wei, R. Pazourek, S. Nagele, C. Ott, C. D. Lin, J. Burgdörfer, and T. Pfeifer, “Observing the ultrafast buildup of a Fano resonance in the time domain.” Science. **354**, 738–741 (2016).
6. K. Klünder, J. M. Dahlström, M. Gisselbrecht, T. Fordell, M. Swoboda, D. Guénot, P. Johnsson, J. Caillat, J. Mauritsson, A. Maquet, R. Taïeb, and A. L’Huillier, “Probing Single-Photon Ionization on the Attosecond Time Scale,” Phys. Rev. Lett. **106**, 143002 (2011).
7. S. Haessler, B. Fabre, J. Higuet, J. Caillat, T. Ruchon, P. Breger, B. Carré, E. Constant, A. Maquet, E. Mével, P. Salières, R. Taïeb, and Y. Mairesse, “Phase-resolved attosecond near-threshold photoionization of molecular nitrogen,” Phys. Rev. A **80**, 011404 (2009).
8. M. Swoboda, T. Fordell, K. Klünder, J. M. Dahlström, M. Miranda, C. Buth, K. J. Schafer, J. Mauritsson, A. L’Huillier, and M. Gisselbrecht, “Phase Measurement of Resonant Two-Photon Ionization in Helium,” Phys. Rev. Lett. **104**, 103003 (2010).
9. J. Caillat, A. Maquet, S. Haessler, B. Fabre, T. Ruchon, P. Salières, Y. Mairesse, and R. Taïeb, “Attosecond Resolved Electron Release in Two-Color Near-Threshold Photoionization of N_2,” Phys. Rev. Lett. **106**, 093002 (2011).
10. D. Guénot, K. Klünder, C. L. Arnold, D. Kroon, J. M. Dahlström, M. Miranda, T. Fordell, M. Gisselbrecht, P. Johnsson, J. Mauritsson, E. Lindroth, A. Maquet, R. Taïeb, A. L’Huillier, and A. S. Kheifets, “Photoemission-time-delay measurements and calculations close to the 3s-ionization-cross-section minimum in Ar,” Phys. Rev. A **85**, 053424 (2012).
11. A. L. Cavalieri, N. Müller, T. Uphues, V. S. Yakovlev, A. Baltuška, B. Horvath, B. Schmidt, L. Blümel, R. Holzwarth, S. Hendel, M. Drescher, U. Kleineberg, P. M. Echenique, R. Kienberger, F. Krausz, and U. Heinzmann, “Attosecond spectroscopy in condensed matter,” Nature **449**, 1029–1032 (2007).

#338236 https://doi.org/10.1364/OE.26.028604
Journal © 2018 Received 11 Jul 2018; revised 18 Aug 2018; accepted 26 Aug 2018; published 19 Oct 2018

12. M. Schultze, M. Fieß, N. Karpowicz, J. Gagnon, M. Korbman, M. Hofstetter, S. Neppl, A. L. Cavalieri, Y. Komninos, T. Mercouris, C. A. Nicolaides, R. Pazourek, S. Nagele, J. Feist, J. Burgdörfer, A. M. Azzeer, R. Ernstorfer, R. Kienberger, U. Kleineberg, E. Goulielmakis, F. Krausz, and V. S. Yakovlev, "Delay in Photoemission," Science **328**, 1658–1662 (2010).
13. E. P. Wigner, "Lower limit for the energy derivative of the scattering phase shift," Phys. Rev. **98**, 145 (1955).
14. C. A. De Carvalho and H. M. Nussenzveig, "Time delay," Phys. Rep. **364**, 83–174 (2002).
15. J. M. Dahlström, A. L'Huillier, and A. Maquet, "Introduction to attosecond delays in photoionization," J. Phys. B **45**, 183001 (2012).
16. R. Locher, M. Lucchini, J. Herrmann, M. Sabbar, M. Weger, A. Ludwig, L. Castiglioni, M. Greif, M. Hengsberger, L. Gallmann, and U. Keller, "Versatile attosecond beamline in a two-foci configuration for simultaneous time-resolved measurements," Rev. Sci. Instrum. **85**, 013113 (2014).
17. M. Huppert, I. Jordan, D. Baykusheva, A. von Conta, and H. J. Wörner, "Attosecond Delays in Molecular Photoionization," Phys. Rev. Lett. **117**, 093001 (2016).
18. S. Heuser, A. Jiménez Galán, C. Cirelli, C. Marante, M. Sabbar, R. Boge, M. Lucchini, L. Gallmann, I. Ivanov, A. S. Kheifets, J. M. Dahlström, E. Lindroth, L. Argenti, F. Martín, and U. Keller, "Angular dependence of photoemission time delay in helium," Phys. Rev. A **94**, 063409 (2016).
19. M. Isinger, R. J. Squibb, D. Busto, S. Zhong, A. Harth, D. Kroon, S. Nandi, C. L. Arnold, M. Miranda, J. M. Dahlström, E. Lindroth, R. Feifel, M. Gisselbrecht, and A. L'Huillier, "Photoionization in the time and frequency domain," Science **358**, 893–896 (2017).
20. L. Gallmann, I. Jordan, H. J. Wörner, L. Castiglioni, M. Hengsberger, J. Osterwalder, C. A. Arrell, M. Chergui, E. Liberatore, U. Rothlisberger, and U. Keller, "Photoemission and photoionization time delays and rates," Struct. Dyn. **4**, 061502 (2017).
21. C. Cirelli, C. Marante, S. Heuser, C. L. M. Petersson, Á. J. Galán, L. Argenti, S. Zhong, D. Busto, M. Isinger, S. Nandi, S. Maclot, L. Rading, P. Johnsson, M. Gisselbrecht, M. Lucchini, L. Gallmann, J. M. Dahlström, E. Lindroth, A. L'Huillier, F. Martín, and U. Keller, "Anisotropic photoemission time delays close to a Fano resonance," Nat. Commun. **9**, 955 (2018).
22. J. Vos, L. Cattaneo, S. Patchkovskii, T. Zimmermann, C. Cirelli, M. Lucchini, A. Kheifets, A. S. Landsman, and U. Keller, "Orientation-dependent stereo wigner time delay and electron localization in a small molecule," Science. **360**, 1326–1330 (2018).
23. L. Cattaneo, J. Vos, R. Bello, A. Palacios, S. Heuser, L. Pedrelli, M. Lucchini, C. Cirelli, F. Martín, and U. Keller, "Attosecond coupled electron and nuclear dynamics in dissociative ionization of H2," Nat. Phys. pp. 733–738 (2018).
24. P. M. Paul, E. S. Toma, P. Breger, G. Mullot, F. Augé, P. Balcou, H. G. Muller, and P. Agostini, "Observation of a Train of Attosecond Pulses from High Harmonic Generation," Science. **292**, 1689–1692 (2001).
25. Y. Mairesse, A. de Bohan, L. J. Frasinski, H. Merdji, L. C. Dinu, P. Monchicourt, P. Breger, M. Kovacev, R. Taïeb, B. Carré, H. G. Muller, P. Agostini, and P. Salières, "Attosecond synchronization of high-harmonic soft x-rays." Science. **302**, 1540–3 (2003).
26. C. Palatchi, J. M. Dahlström, A. Kheifets, I. Ivanov, D. Canaday, P. Agostini, and L. DiMauro, "Atomic delay in helium, neon, argon and krypton," J. Phys. B **47**, 245003 (2014).
27. I. Jordan and H. J. Wörner, "Extracting attosecond delays from spectrally overlapping interferograms," J. Opt. **20**, 024013 (2018).
28. J. Wätzel, A. S. Moskalenko, Y. Pavlyukh, and J. Berakdar, "Angular resolved time delay in photoemission," J. Phys. B **48**, 025602 (2015).
29. A. Kheifets, A. Mandal, P. C. Deshmukh, V. K. Dolmatov, D. A. Keating, and S. T. Manson, "Relativistic calculations of angle-dependent photoemission time delay," Phys. Rev. A **94**, 013423 (2016).
30. I. A. Ivanov and A. S. Kheifets, "Angle-dependent time delay in two-color xuv+ir photoemission of he and ne," Phys. Rev. A **96**, 013408 (2017).
31. M. Sabbar, S. Heuser, R. Boge, M. Lucchini, L. Gallmann, C. Cirelli, and U. Keller, "Combining attosecond XUV pulses with coincidence spectroscopy," Rev. Sci. Instrum. **85**, 103113 (2014).
32. M. Schultze, A. Wirth, I. Grguras, M. Uiberacker, T. Uphues, A. Verhoef, J. Gagnon, M. Hofstetter, U. Kleineberg, E. Goulielmakis, and F. Krausz, "State-of-the-art attosecond metrology," J. Electron. Spectrosc. Relat. Phenom. **184**, 68–77 (2011).
33. M. Huppert, "Actively-Stabilized Attosecond Beamline and Its Application to Attosecond Dynamics in Atoms, Molecules, and Liquids," Ph.D. thesis, ETH Zürich (2016).
34. M. Drescher, M. Hentschel, R. Kienberger, M. Uiberacker, V. Yakovlev, a. Scrinzi, T. Westerwalbesloh, U. Kleineberg, U. Heinzmann, and F. Krausz, "Time-resolved atomic inner-shell spectroscopy." Nature. **419**, 803–7 (2002).
35. I. Jordan, A. Jain, T. Gaumnitz, J. Ma, and H. J. Wörner, "Photoelectron spectrometer for liquid and gas-phase attosecond spectroscopy with field-free and magnetic bottle operation modes," Rev. Sci. Instrum. **89** (2018).
36. V. Véniard, R. Taïeb, and A. Maquet, "Phase dependence of (N+1)-color (N>1) ir-uv photoionization of atoms with higher harmonics," Phys. Rev. A **54**, 721 (1996).
37. E. Seres, J. Seres, F. Krausz, and C. Spielmann, "Generation of coherent soft-x-ray radiation extending far beyond the titanium L edge," Phys. Rev. Lett. **92**, 163002 (2004).
38. T. Popmintchev, M.-C. Chen, D. Popmintchev, P. Arpin, S. Brown, S. Ališauskas, G. Andriukaitis, T. Balčiunas, O. D. Mücke, A. Pugzlys, A. Baltuška, B. Shim, S. E. Schrauth, A. Gaeta, C. Hernández-García, L. Plaja, A. Becker,

A. Jaron-Becker, M. M. Murnane, and H. C. Kapteyn, “Bright coherent ultrahigh harmonics in the keV x-ray regime from mid-infrared femtosecond lasers,” Science. **336**, 1287–1291 (2012).

39. D. Guénot, D. Kroon, E. Balogh, E. W. Larsen, M. Kotur, M. Miranda, T. Fordell, P. Johnsson, J. Mauritsson, M. Gisselbrecht, K. Varjù, C. L. Arnold, T. Carette, A. S. Kheifets, E. Lindroth, A. L’Huillier, and J. M. Dahlström, “Measurements of relative photoemission time delays in noble gas atoms,” J. Phys. B **47**, 245602 (2014).
40. M. Sabbar, S. Heuser, R. Boge, M. Lucchini, T. Carette, E. Lindroth, L. Gallmann, C. Cirelli, and U. Keller, “Resonance effects in photoemission time delays,” Phys. Rev. Lett. **115**, 133001 (2015).
41. A. Jain, T. Gaumnitz, A. Bray, A. Kheifets, and H. J. Wörner, “Photoionization delays in xenon using single-shot referencing in the collinear back-focusing geometry,” Opt. Lett. **43** (2018).
42. J. B. West and G. V. Marr, “The absolute photoionization cross section of helium, neon, argon and krypton in the extreme vacuum ultraviolet region of the spectrum,” Proc. Royal Soc. A **349**, 397–421 (1976).
43. I. Velchev, W. Hogervorst, and W. Ubachs, “Precision VUV spectroscopy of Ar I at 105 nm,” J. Phys. B **32**, L511–L516 (1999).
44. W. C. Martin, “Energy Levels and Spectrum of Neutral Helium (^{4}He I),” J. Res. Natl. Bur. Stand. Sect. A **64A**, 19 (1960).
45. P. J. Linstrom and W. G. Mallard, “The NIST Chemistry WebBook: A chemical data resource on the Internet,” J. Chem. Eng. Data **46**, 1059–1063 (2001).
46. V. Kaufman and L. Minnhagen, “Accurate Ground-Term Combinations in Ne I,” J. Opt. Soc. Am. **62**, 92 (1972).
47. A. Kheifets, “Time delay in valence-shell photoionization of noble-gas atoms,” Phys. Rev. A **87**, 063404 (2013).
48. R. Pazourek, S. Nagele, and J. Burgdörfer, “Attosecond chronoscopy of photoemission,” Rev. Mod. Phys. **87**, 765–802 (2015).
49. A. W. Bray, F. Naseem, and A. S. Kheifets, “Simulation of angular resolved RABBITT measurements in noble gas atoms,” Phys. Rev. A **97**, 063404 (2018).
50. K. Kimura, S. Katsumata, Y. Achiba, T. Yamazaki, and S. Iwata, *Handbook of HeI Photoelectron Spectra of Fundamental Organic Molecules* (Japan Scientific Societies Press, Tokyo, 1981).

---

1. Introduction

Attosecond spectroscopy has given insight into the fundamental properties of atoms and molecules [1–5]. Measurement techniques like reconstruction of attosecond beating by interference of two-photon transitions (RABBITT) [6–10] and attosecond streaking [11, 12] have made the relative Wigner time-delays τ_W [13] between different orbitals of atoms and molecules accessible. Several pioneering experiments [6, 11, 12] have employed isolated attosecond pulses (IAP) and attosecond pulse trains (APTs) to resolve photoemission time-delays [13–23] in atoms, molecules and solids.

The RABBITT technique involves quantum path interference [24, 25] using an attosecond pulse train consisting of odd harmonics used as pump to ionize the atoms/molecules and the fundamental laser field as a probe. Photoionization by XUV with photon energy $E_{h\nu}$ results in principal photoelectron peaks at the corresponding photoelectron kinetic energies $E_{\mathrm{kin}} = E_{h\nu} - \mathrm{IP}$, where IP is the ionization potential of the target. Due to the generation process itself, several harmonic orders are generated up to the cut-off energy $E_{\mathrm{cut-off}} \propto 3.17 I \lambda_{\mathrm{L}}^2$, where λ_{L} is the central wavelength of the driving laser and I its peak intensity. In the simplest case, N odd harmonic orders in the frequency domain translate to $N \times M$ principal photoelectron peaks in the photoelectron energy domain, where M is the number of orbitals that can be photo-ionized. The presence of the IR field at frequency ω_{L} results in degenerate quantum paths from consecutive high-harmonic (H) orders spaced by $2\omega_{\mathrm{L}}$ and therefore in sidebands (SBs) in the photoelectron spectrum. This results in $(N + (N - 1)) \times M$ peaks in the photoelectron spectrum. The Spectral congestion increases with larger values of N and M. Therefore, spectral overlap of photoemission lines from different orbitals due to many harmonic orders is a shortcoming of this method that has limited RABBITT measurements to low photon energies.

Till now, only thin metallic foils, that act as bandpass filters for the XUV radiation, have been employed to select the photon energy and restrict the number of contributing odd high-harmonic orders for the pump-probe experiment. Klünder *et al.* [6] used chromium to select a 10 eV broad spectral range at 38 eV central energy to avoid spectral overlap between the measured photoemission lines. Palatchi *et al.* [26] presented the effective Wigner delay for different noble gases (Ne, Ar, Kr) up to a maximum photon energy of around 75 eV. Huppert *et al.* [17] also employed spectral filtering using several metal filters (Sn, Cr, Ti) at EUV energies up to 37 eV photon energy. This poses limitations on the highest photon energy that can be used for RABBITT measurements, as it requires metallic foils with a restricted bandwidth and reasonable transmission. This selectivity is not available for all photon energies, as the transmission is a property of the filter material.

Recently, Isinger and co-workers [19] discussed photoionization in time- and frequency-domain, where they used the RABBITT technique, and extracted photoionization delays for neon with high temporal resolution of 20 as and 200 meV spectral accuracy. Two Zr foils of 200 nm thickness each have been used to select the photon energy region ranging from around 65 eV up to 105 eV. Neon is a very special case as the ionization potential between the different levels of neon ($IP_{2p} = 21.6$ eV, $IP_{2s} = 48.5$ eV) is approximately 27 eV. By restricting the highest photon energy to around 105 eV, minimum overlap between photoelectrons from harmonic lines and sideband peaks from different orbitals of neon was ensured. However, this scheme is not applicable in general as already for argon and an argon-neon gas mixture the difference in IP of the neighboring orbitals decreases to 14 eV and 6 eV, respectively. This results in overlapping spectral contributions and a very complex photoelectron spectrum and RABBITT trace. Reconstruction schemes [27] handling these complex spectra have been recently proposed. Here, we follow a different experimental approach, which enables clean RABBITT traces, and hence makes them easier for data analysis and less prone to analysis errors.

We present and experimentally demonstrate a novel scheme to systematically study the energy-dependent photoemission time-delays, with a further possibility to access angular resolved photoemission time-delays [28–30], for atoms, gases and liquids. Up to now, RABBITT attosecond interferometry experiments have been done in forward focusing geometry [16, 17, 19, 21, 31] with the energy of the harmonic order mainly tuned with the laser intensity, the generation gas pressure and bandpass filtering of the harmonic spectrum with thin metallic filters. Here we introduce a different way to exploit the energy-dependence of the photoemission delays using a back-focusing multilayer mirror [32] where the central XUV energy can be selectively implemented. An important feature is the bandwidth of the mirror which can be tuned by the amount of layers in the mirror stack to restrict the reflection to just two consecutive odd harmonic orders (corresponding to $\Delta E_{\mathrm{ML}} \approx 5$ eV at $\lambda_{\mathrm{L}}=795$ nm). This results in just one single oscillating sideband for a particular pair of photoemission lines. This feature has therefore allowed us to access photoemission time delays using the RABBITT scheme at $E_{\mathrm{XUV}} \approx 90$ eV central photon energy. The setup will allow access to delays at even higher photon energies, which were difficult to reach so far due to spectral overlap of the photoelectrons generated from different orbitals. To demonstrate the applicability of our method, we have used gas mixtures, e.g. Ar-Ne and Ar-He.

Referencing the phase between sidebands associated with different photoemission lines in simultaneous measurements of two species simply cancels out all the common terms, including the spectral phase of the XUV pulse train and results in the direct measurement of the phase shift between the involved photoemission lines. Having just two harmonic lines reduces the complexity of overlapping contributions in the spectrum, coming from both principal harmonic photoelectron peaks and the IR induced sidebands, to the minimum. This allows to expose gas mixtures to the same XUV pulse, allowing cancellation of the high-harmonic chirp (or elimination of the influence of XUV pulse) and resulting in the measurement of absolute delay differences between different gas targets. We present simulations to show the applications of this method to molecules and how it can be used to benchmark delays from molecules to helium. This scheme is an important realization which will make the delay measurements at all photon energies possible.

Section 2 contains a detailed description of our attosecond beamline used for the experiment. In Section 3, we simulate RABBITT traces for valence shells of rare gas atoms and gas mixtures by using only metallic foils and compare it to our new scheme, where we select just two harmonic lines. We further compare these simulations to our measured interferograms and access the photoemission delays. In Section 4, we discuss the obtained results in the context of existing theory and exemplify our scheme for molecule-gas mixtures in Section 5. In Section 6, we discuss the conclusions and give an outlook on applications to molecules, solids and liquids.

2. Experimental setup

The schematic of our experimental setup is shown in Fig. 1(A). A 1 kHz, Ti:Sapphire laser system consisting of a Femtolasers Rainbow 4 oscillator with feed-forward CEP stabilization and a Femtolasers Femtopower V pro (1 kHz, 5.5 mJ) amplifier is used for high-harmonic generation. The output after the amplifier and the grating compressor is characterized using a fringe autocorrelator to a pulse duration of $\tau_L \approx 25$ fs. The laser pulses are centered at $\lambda_L = 795$ nm, where about 700 μJ of the total pulse energy is guided to the beamline. A $\lambda/2$-waveplate can be introduced into the IR beam path for angular resolved measurements. The full beam ($F^{\#} \approx 40$) is focused onto a helium gas target for high-harmonic generation, shown in Fig. 2. The generation target is a differentially pumped gas cell described in section 2.1.

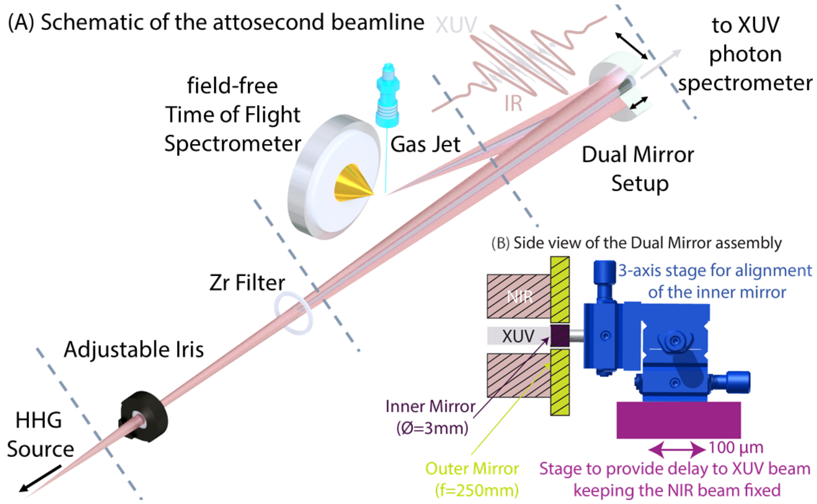

Fig. 1. Attosecond beamline and dual mirror assembly. (A) Schematic of the attosecond pump-probe beamline consisting of five blocks demarcated by dashed lines: (i) differentially pumped high-harmonic generation source, (ii) Zr filter for XUV filtering and iris for IR control, (iii) Dual mirror assembly for XUV-IR delay, (iv) XUV spectrometer for HHG/XUV diagnostics, (v) Interaction chamber and field-free time-of-flight spectrometer for photoelectron detection and measurement. (B) Cross-sectional view of the dual mirror delay setup: An outer annular mirror with 3.5 mm hole and 25 cm focal length for IR focusing and an inner multilayer mirror with 3 mm diameter for reflection of XUV. The inner mirror is mounted on a three-axis manual translation stage for coarse alignment with respect to the outer mirror. A piezo-linear stage provides the delay between the IR and the XUV pulse.

2.1. *Differentially pumped finite gas target*

The target for high-harmonic generation consists of a stainless steel tube with variable inner diameters from 2 to 7 mm. For the interaction of the laser with the target, holes are drilled into the tube walls in-situ by the laser beam itself, such that the alignment effort is minimized and a minimal hole diameter is achieved, thereby ensuring an optimal target-laser interaction area. It has been observed that higher gas pressures in the target can be achieved in comparison with the pre-drilled holes. The backing pressure of the target tube is adjusted using a fine adjustment needle valve (Pfeiffer EVN 116) and measured using a capacitive pressure gauge (Pfeiffer CMR 361) to enable measurements for different target gases [33]. To minimize re-absorption of the generated EUV/XUV radiation due to the high pressure of the gas used, two stages of differential pumping are implemented. It is also important for few-cycle high intensity laser beams, to ensure that the laser beam does not interact with the gas in the path before it is focused in the designated interaction region. The target tube is, therefore, mounted inside a cube with an opening of ($\varnothing \approx 0.5-1$ mm), adapted to the input laser parameters and the focal length of the focusing optics, in the propagation direction and view-port on the top to optimize the laser alignment and observe plasma formation. For easy alignment of the cube with respect to the laser, a movable kick-off mirror in the path is used to image the beam and optimize for the maximum IR transmission and alignment through the generation gas target. For high pressure targets, a skimmer can be inserted into the chamber exit for differential pumping. The cube is connected to a roughing vacuum pump, which allows to reduce the pressure inside the cube already to 0.1 mbar and reduce re-absorption. A three-axis translation stage allows alignment of the laser through the holes in the cube and also the positioning of the focus of the beam for XUV flux and shape optimization. The surrounding vacuum chamber is pumped by a turbo-molecular pump (Pfeiffer HiPace 300) to maintain the pressure below 1e-3 mbar during operation and <1e-6 mbar with no gas load.

For the experiments described in section 3, gas pressures of around 700-1000 mbar for He and a propagation length of 3-4 mm in the generation medium, resulted in the maximum XUV flux in the spectral region of interest, here 80-100 eV, as shown in Fig. 2.

2.2. XUV beam/pulse shaping and diagnostics

Both beams, the residual IR beam from high-harmonic generation and the XUV beam, co-propagate together towards a dual mirror assembly as shown in Fig. 1. While propagating, the collinear beams pass through a motorized iris (Smaract) for precise adjustment with respect to the XUV beam, mounted on a two-axis linear stage for controlling the IR intensity and hence the sideband amplitude for RABBITT experiments as single IR photon absorption is required for a reliable data analysis. Also, it controls the above-threshold ionization (ATI) electrons which contribute to an unwanted background signal in RABBITT measurements. The beams then propagate through a multi-filter setup, which allows variable filters for static and time-resolved PES measurements. The multi-filter setup is a motorized filter holder assembly, that allows up to four filters. For static measurements, metallic foils Al/Zr (0.1/0.2μm thickness), 10 mm diameter (Lebow Company) are used. For time-resolved measurements, a free-standing metal-foil (Zr 100-200 nm) of about 3 mm diameter is mounted on thin tungsten wires. This results in an annular IR beam, where only the HHG/XUV beam remains in the center. The chamber also contains optics for imaging the reflected beam from the dual mirror assembly after the focus. This reflected beam is imaged onto a camera for spatial and temporal overlap of the XUV and the IR [32]. The chamber is therefore referred to as the diagnostics chamber.

2.3. Delay generation and passive-stabilization

The two beams further propagate to the dual mirror assembly [34], where the inner mirror (Ultrafast Innovations) is a XUV multilayer mirror (d=3 mm, f=250 mm), shown in Fig. 1(B). The inner mirror can be centered with respect to the outer mirror that is mounted on a home-made gimbal mount, with a manual three-axis linear translation stage. The delay between the inner and outer-reflected beam is adjusted by a piezo-linear stage (Physik Instrumente E709 digital piezo-controller with capacitive encoder, P-611.1S) along the propagation direction. It is used to adjust the delay between the XUV, focused using the inner mirror, and the IR beam, focused using the outer mirror. The whole dual mirror assembly is mounted on a stage for translation perpendicular to the propagation direction, which allows moving the assembly out of the beam path for XUV source characterization. The beamline is intrinsically stable as XUV and IR beams are propagating (with different divergence) along the same beam path and are therefore influenced in the same way. The stability is essential to perform attosecond pump-probe experiments.

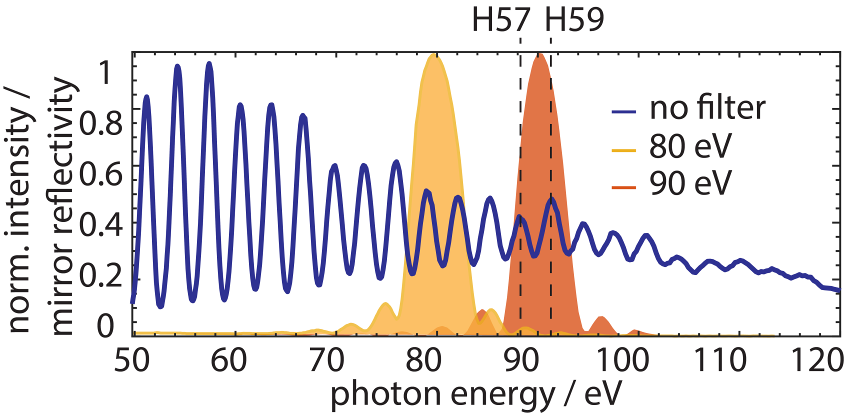

Fig. 2. High-harmonic spectrum and multilayer mirror reflectivity. High-harmonic spectrum obtained in helium. The normalized mirror reflectivity curves for a $\Delta E_{\mathrm{ML}} \approx 5\,\mathrm{eV}$ broad XUV mirror centered at $E_{\mathrm{XUV}} = 80\,\mathrm{eV}$ and 90 eV are overlaid on the harmonic spectrum. Two harmonic orders can be selectively chosen by changing the central energy of the XUV mirror.

2.4. XUV spectrometer for HHG diagnostics

The relative flux and beam characteristics of the XUV source are optimized using a flat-field grating XUV spectrometer. Due to the high nonlinearity of the HHG process a careful adjustment of the generation conditions is required. The photon flux and spatial profile depend on the generation conditions in the gas cell like gas pressure, length of the gas target and laser intensity in the gas medium. A home-made grating based XUV photon spectrometer [33] is used to optimize and monitor the high-harmonic spectrum generated in the gas target. An adjustable slit is used to control the spectrometer resolution versus photon flux. A diffraction grating (Shimadzu 30-002, 1200 lines/mm, variable line spacing flat field laminar type) diffracts the beam onto a chevron-type micro-channel plate (Beam Imaging Solutions, BOS-40-IAA-CH-MS), where the spectrum is converted on a phosphor screen (P-43, peak wavelength: 540 nm) to the visible, which is imaged by a CCD-camera (PCO Edge).

The motorized iris in the diagnostics chamber is centered for the maximum flux of the XUV source. This is later used as the reference to center the dual mirror assembly.

2.5. Interaction region

After careful optimization of the HHG spectrum in the desired spectral region, the dual mirror is moved into the beam path using a linear translation stage, such that the XUV is centered on the inner mirror. The apparatus was designed such that for an angle of incidence (AOI) of 2.5° with respect to the target normal, the beam is focused in front of the time-of-flight (TOF) spectrometer. Perpendicular to the TOF axis and the laser beam, a grounded metallic effusive-nozzle is installed to provide the highest target density in the interaction region. The nozzle can be adjusted using a three-axis linear positioner (Smaract) with encoder for highest repeatability. The TOF spectrometer is described in more detail in [35]. The spectrometer is optimized for field-free (FF-TOF mode) type measurements and also for low-flux measurements (magnetic-bottle-type operation) for both gases and liquids. It includes the option for retardation to achieve optimal resolution (e.g. between H and SB) in a certain energy range. A small entrance ($\varnothing \approx 500\,\mu$m) aperture of the TOF tube allows the benefit of differential pumping and small acceptance angle for higher resolution in angular-resolved measurements.

3. Results

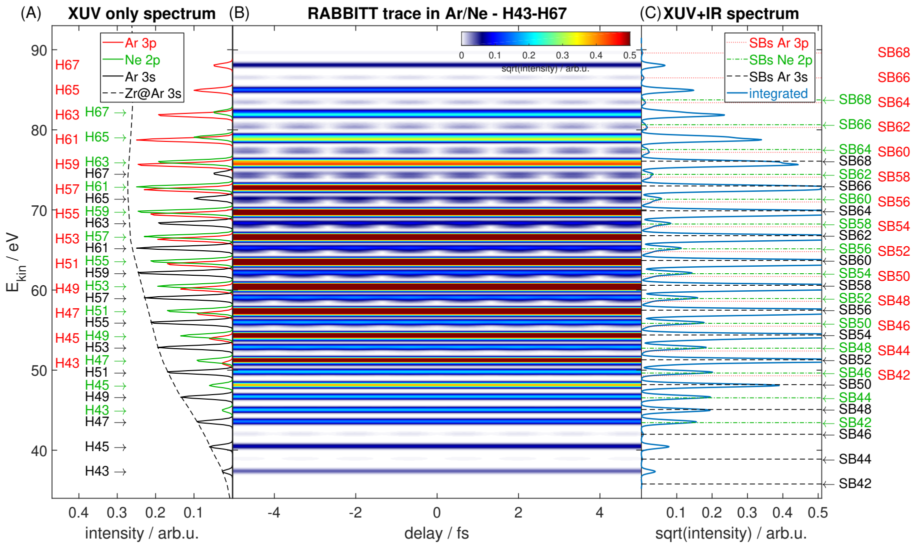

Fig. 3. Calculated RABBITT trace for an argon-neon mixture at high photon energies. (A) Photoelectron distribution for XUV only ionization from an argon-neon mixture. Two thin (200 nm) Zr filters are used as a high-pass filter (transmission curve: dashed line, cf. CXRO) to select the harmonic orders H43 to H67 of 800 nm fundamental radiation. Ionization of Ar 3p (IP=15.8 eV) (red), Ar 3s (IP=29.3 eV) (black), and Ne 2p (IP=21.65 eV) (green). (B) XUV-IR pump-probe delay scan, showing the RABBITT trace for the Ar-Ne mixture. Spectral overlap and congestion is clearly visible for several sidebands (e.g. SB42 to SB68). (C) Photoelectron signal from (B) integrated over the time delay (blue) together with the theoretical SB positions for Ar 3p (black dashed), 3p (red dotted), and the Ne 2p (green dash dotted) photoemission lines.

The experimental setup allows to probe one of the most fundamental processes of photoemission occurring on attosecond timescales. The RABBITT technique was first proposed by Veniard *et al.* [36] in 1996 and demonstrated by Paul *et al.* [24] in 2001. All measurements using the RABBITT technique have been limited to low photon energies even though the HHG sources have been used for a long time to generate EUV photons in the range up to 1.6 keV [37, 38].

In this article, we present RABBITT experiments in neon-argon and helium-argon gas mixtures. We demonstrate the access to delays at high photon energies of $E_{\mathrm{XUV}} \approx 90$ eV, with the advantage of extending the scheme to even higher photon energies, where the spectral filtering can not be easily performed using thin metallic foils, e.g. due to low flux and high absorption of multiple-foil stacks, with the additional ability to choose the photon energy of interest. The experiments to obtain the relative photoionization delays have been performed by introducing the gases simultaneously and exploiting the bandwidth of the mirror. To obtain the highest precision and stability for the photoionization delays between different types of gases, gas mixtures are employed allowing for simultaneous rather than consecutive measurements [39].

Previously, Guénot *et al.* [39] measured relative photoemission delays between the outer valence bands of argon, helium and neon in the photon energy range 31 to 37 eV. Their scheme uses four consecutive harmonics that requires a difference of almost 12.5 eV in the IP of different gases to avoid overlap between the spectra. This is not the case for gas mixtures of Ar, Ne and He. Therefore, they innovatively performed consecutive RABBITT scans with alternating gases and repeated the measurements many times to compensate for any external drifts during the measurement. They observed a statistical error for each scan of around 25 as. The drift observed in the experimental results is accounted for as a laser/beamline drift that is assumed to be linear in time and quantified by fitting the drift in two gases simultaneously. As an alternative approach, Sabbar *et al.* [40] reported simultaneous streaking measurements on argon and neon using electron-ion coincidences in a cold target recoil ion momentum spectrometer (COLTRIMS) setup.

As we discussed earlier, RABBITT measurements in neon at high photon energies demonstrated in [19] are a very special case as the difference in IP for the two valence orbitals of neon is ≈ 27 eV. Here, we investigate the limitations of this scheme by simulating the RABBITT spectrogram for a neon-argon gas mixture, shown in Fig. 3. This simulation assumes N=13 consecutive odd harmonic orders, ranging from H43 to H67. The harmonics are chosen similar to [19] by including the transmission of the Zr foil in the simulation. For each odd harmonic order, there are $N \times M = 13 \times 3$ principal peak contributions (cf. Fig. 3(A)) and $(N-1) \times M = 12 \times 3$ sideband contributions (cf. Fig. 3(C)) in the photoelectron spectra. This leads to a highly congested photoelectron spectrum even for rare gases.

Our experimental scheme provides a novel solution to these issues. An attosecond pulse train (APT) consisting of two harmonic orders is reflected from the XUV multilayer mirror. For the here presented experiments, the XUV mirror is centered at $E_{\mathrm{XUV}} \approx 90$ eV with a $\Delta E_{\mathrm{ML}} \approx 5$ eV bandwidth. Discrete photoelectrons corresponding to the odd harmonic orders, H57 and H59 of IR fundamental frequency of 1.55 eV separated by $2\hbar\omega_{\mathrm{L}}$, where $\hbar$ is the reduced Planck constant and ω_{L} is the IR fundamental frequency, are generated in the target gas.

Figure 4 shows a simulated RABBITT trace for a neon-argon mixture with harmonic orders 57 and 59. For two harmonic orders, there are $N \times M = 2 \times 3$ principal peak contributions (cf. Fig. 4(A)) and $(N-1) \times M = 1 \times 3$ sideband contributions (cf. Fig. 4(C)) in the photoelectron spectra. There is no spectral overlap between neighbouring lines, clearly demonstrating the advantage over the scheme limited by the use of metallic foils only. Our scheme, therefore, presents a simpler, faster measurement scheme, allowing the measurements at different photon energies with the use of different multilayer mirrors. Recently, photoionization delays from the 4d subshell of xenon have been accessed by implementation of single-shot referencing in this collinear back-focusing geometry [41].

3.1. Static photoelectron spectra

Here we present our experimental results. To demonstrate the selectivity of two harmonics at the required energies, we present the static photoelectron spectra measured in argon, neon, helium, an argon-neon mixture in the ratio 3:1 and an argon-helium mixture (ratio 1:3) in Fig. 5. The ratios are chosen to yield similar photoelectron signals, determined by the relative photoionization cross sections at 90 eV [42]. The field-free time-of-flight spectrometer is calibrated by using the Auger electrons emitted from the photoionization of xenon.

Using our 90 eV multilayer mirror, harmonic orders H57 and H59 are reflected while the other harmonics are suppressed as shown in Fig. 5. Obtaining just two harmonic lines for RABBITT is therefore an advantage, to avoid overlap for multiple photoemission lines from different gases. For example, $\mathrm{He}_{1\mathrm{s}}$ (IP=24.6 eV) and $\mathrm{Ar}_{3\mathrm{p}}$ (IP=15.8 eV) [43–45] are separated by three harmonic orders. The outer valence shells of $\mathrm{Ne}_{2\mathrm{p}}$ (IP=21.6 eV) and $\mathrm{Ar}_{3\mathrm{p}}$ (IP=15.8 eV) [43, 45, 46] are separated by the equivalent of about two harmonic orders, where the resolving ability is provided by the restricted XUV reflection bandwidth.

The spectra for Ar, Ar-He mixture and Ar-Ne mixture are obtained with a deceleration of

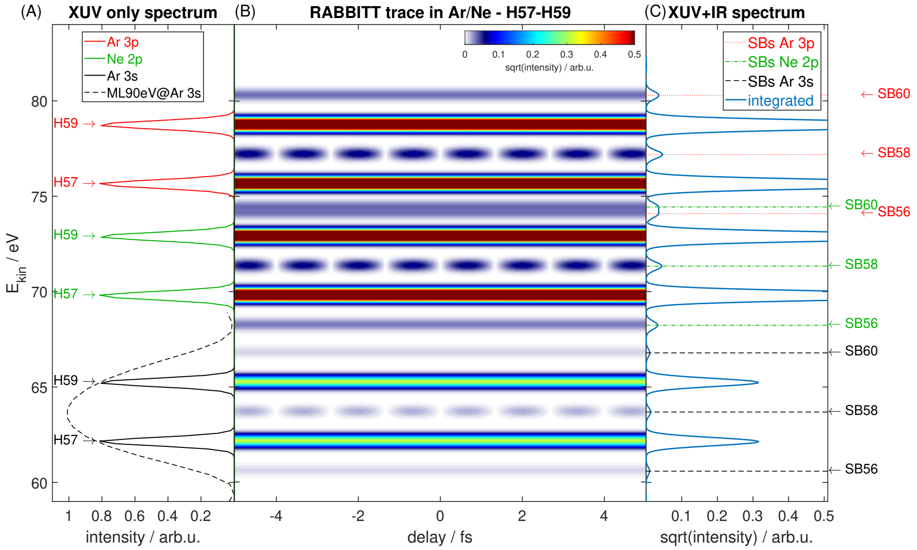

Fig. 4. Calculated RABBITT trace for an argon-neon mixture at high photon energies for two harmonic lines. (A) Photoelectron distribution for XUV only ionization from an argon-neon mixture. A multilayer mirror centered at $E_{\mathrm{XUV}} \approx 90\,\mathrm{eV}$ with a bandwidth of $\Delta E_{\mathrm{ML}} \approx 5\,\mathrm{eV}$ is used to select the harmonic orders H57 to H59 from an HHG comb with 800 nm as the fundamental radiation. (B) XUV-IR pump-probe delay scan, showing the RABBITT trace for the Ar-Ne mixture, where well-resolved SB oscillations are visible. (C) Photoelectron signal from (B) integrated over the time delay (blue) together with the theoretical SB positions for Ar 3p (black dashed), 3p (red dotted), and the Ne 2p (green dash dotted) photoemission lines.

$U_{\mathrm{ret}} = 47\,\mathrm{V}$ and for Ne and He photoemission signals, a deceleration of $U_{\mathrm{ret}} = 35\,\mathrm{V}$ is applied to remove the low-energy background. A coil current of $I_{\mathrm{coil}} = 0.3\,\mathrm{A}$ is used to increase the collection efficiency. Characterization of retardation and amplification properties of the TOF have been discussed in [35].

3.2. RABBITT for gas mixtures

In this section we present differences in photoemission delays between outer-shell electrons of argon (3p), neon (2p) and helium (1s). Using the RABBITT interferometric technique, the high-order harmonics H57 and H59 ionize the medium in the presence of a weak IR field. Absorption or emission of one IR photon leads to sidebands in the photoelectron spectra. Due to two contributing pathways, the sideband photoelectron signal modulates as a function of the IR-XUV delay, denoted by τ. The sideband modulation [24, 25] can be expressed as

$$\mathrm{SB}_{\mathrm{orb}} \propto \cos\left(2\omega_{\mathrm{L}}\tau - \Delta\phi_{\mathrm{H}} - \Delta\phi_{\mathrm{atomic}}\right). \tag{1}$$

where τ is the delay between the IR and the XUV pulse. $\Delta\phi_{\mathrm{H}}$ is the difference in spectral phases of two consecutive harmonics, here H57 and H59. $\Delta\phi_{\mathrm{atomic}}$ is usually referred to as the atomic phase difference, which includes the Wigner time-delay τ_{W} due to the process of photoionization itself and the continuum-continuum delay τ_{CC}. τ_{W} has been understood as the group delay of the outgoing electronic wavepacket under the influence of the atomic potential compared to a free electron. The relation between τ_{atomic}, τ_{W} and τ_{CC} can be expressed as [15, 47, 48]:

$$\tau_{\mathrm{atomic}} = \tau_{\mathrm{W}} + \tau_{\mathrm{CC}}. \tag{2}$$

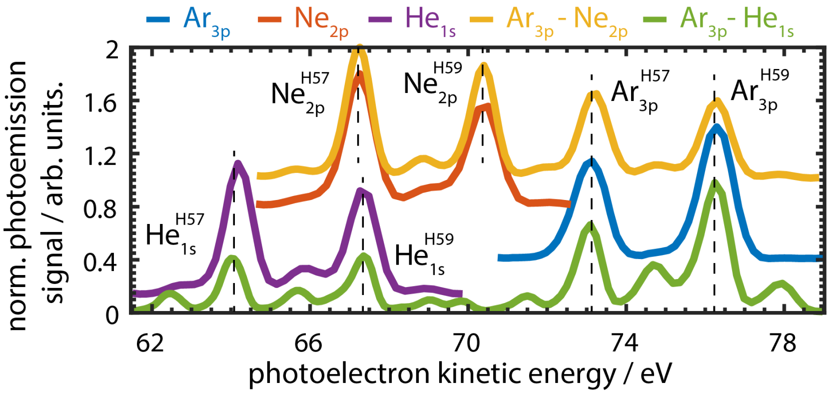

Fig. 5. Retardation-corrected photoelectron spectra. High-harmonic photoelectron spectra from Ar_{3p} (blue), Ne_{2p} (red), He_{1s} (purple), He_{1s}-Ar_{3p} (green) and Ne_{2p}-Ar_{3p} (orange). The spectra have been shifted to the original photoelectron kinetic energy axis by compensating for the retardation potential applied in the time-of-flight spectrometer. The multilayer mirror allows for the selection of harmonic orders H57 and H59. This results in overlap-free photoelectron signal in gas mixtures.

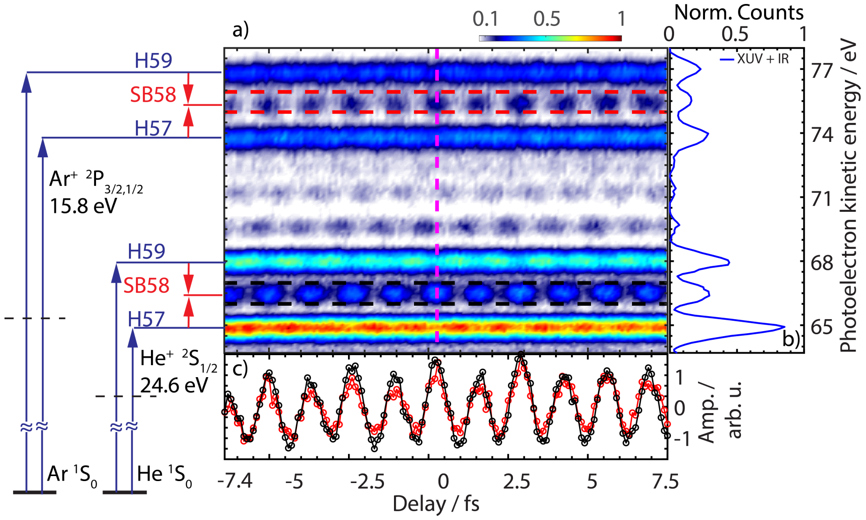

Fig. 6. RABBITT in an Ar-He mixture. (a) RABBITT trace measured in an argon-helium gas mixture (b) A cross-cut of the photoelectron spectra corresponding to the magenta line in (a).The oscillating sideband SB58 for argon (red) and helium (black) as a guide to the eye is shown in (c). This is obtained by averaging the sideband signal for argon and helium in (a) between the dashed lines (red and black respectively).

The relative photoemission time-delay can be extracted as follows [6, 10, 39]:

$$\tau_{\mathrm{Ar}_{3\mathrm{p}}} - \tau_{\mathrm{Ne}_{2\mathrm{p}}} = \frac{\Delta\phi_{\mathrm{Ar}_{3\mathrm{p}}} - \Delta\phi_{\mathrm{Ne}_{2\mathrm{p}}}}{2\omega_{\mathrm{L}}} \quad \text{and} \quad \tau_{\mathrm{Ar}_{3\mathrm{p}}} - \tau_{\mathrm{He}_{1\mathrm{s}}} = \frac{\Delta\phi_{\mathrm{Ar}_{3\mathrm{p}}} - \Delta\phi_{\mathrm{He}_{1\mathrm{s}}}}{2\omega_{\mathrm{L}}} \tag{3}$$

since τ and $\Delta\Phi_{\mathrm{H}}$ cancel out as the atomic orbitals are ionized by the same harmonics as the influence of XUV pulse parameters is the same for both.

In our experiments, due to the high photon energy of $E_{\mathrm{XUV}} \approx 90\,\mathrm{eV}$ and low binding energy of the outer valence electrons, a retardation voltage has been applied for sufficiently high energy resolution. To record the RABBITT trace for outer valence orbitals, i.e., 3p and 3s, of argon, simultaneously with helium, maintaining the maximal possible resolution, a deceleration (retardation) of $U_{\mathrm{ret}} = 47\,\mathrm{V}$ is applied to increase the resolution of the recorded spectrogram. In Fig. 6, the spectrum has been shifted back (by 47 eV) to the photoelectron kinetic energy by compensating for the retardation and matches well with the known IPs. A coil current of $I_{\mathrm{coil}} = 0.3\,\mathrm{A}$ is applied to enhance the collection efficiency. Fig. 6(A) shows the RABBITT measurement for SB58 in an argon-helium gas mixture. The selection of two harmonics and the separation of IP between Ar and He allows for overlap-free traces. A projection of photoelectron spectra, measured at the magenta dashed line is shown in Fig. 6(B). As the measured sidebands are overlap-free, the measurement allows for a simple determination of phase shift between the SB58 of $\mathrm{He}_{1\mathrm{s}}$ and $\mathrm{Ar}_{3\mathrm{p}}$. The relative phases between the side-band oscillations $\Phi_{\mathrm{Ar}_{3\mathrm{p}}} - \Phi_{\mathrm{He}_{1\mathrm{s}}}$ for the sideband order SB58 are determined with the procedure explained below.

We can select the spectral area of interest and extract the phase information in that particular sideband. Taking the relative phase information between the sidebands from different atoms, provides the relative time-delay between the two-photon ionization processes. Here, we follow the complex-fit approach [27]. The RABBITT spectrogram is Fourier-transformed along the XUV-IR delay axis. A one-dimensional array along the photoelectron kinetic energy axis is obtained by integrating the Fourier-transformed spectra around the $2\omega_{\mathrm{L}}$ oscillation frequency. The phases of interest are retrieved by assigning a complex-fit parameter to each photoelectron band and sideband and performing a multi-component fit for each band. The phases obtained for the two discussed experiments are inherently referenced, as we obtain the delay $\tau_{\mathrm{Ar}_{3\mathrm{p}}} - \tau_{\mathrm{He}_{1\mathrm{s}}}$. A similar procedure is used to obtain the delay $\tau_{\mathrm{Ar}_{3\mathrm{p}}} - \tau_{\mathrm{Ne}_{2\mathrm{p}}}$ between sideband oscillations for $\mathrm{Ne}_{2\mathrm{p}}$ and $\mathrm{Ar}_{3\mathrm{p}}$.

As the sidebands for $\Phi_{\mathrm{Ar}_{3\mathrm{p}}}$, $\Phi_{\mathrm{Ne}_{2\mathrm{p}}}$ and $\Phi_{\mathrm{He}_{1\mathrm{s}}}$ are formed with the same harmonic orders, the contribution to phase from the difference in spectral phases of the involved harmonics cancels out, allowing exclusive extraction of the phase difference of $\mathrm{Ar}_{3\mathrm{p}}$, $\mathrm{Ne}_{2\mathrm{p}}$ and $\mathrm{He}_{1\mathrm{s}}$. This method, therefore, allows to systematically extract the energy-dependent delays with high fidelity and high signal-to-noise ratio. The time-delays can then be extracted from the phase delays of the beating patterns using: $\delta\tau = \Delta\phi/(2\omega_{\mathrm{L}})$.

4. Discussion

Table 1 presents the calculated Wigner time delays τ_{W} using the random-phase approximation with exchange (RPAE) method as obtained from [47] and continuum-continuum (cc) corrections τ_{CC} for neon, argon and helium. The results of the delay differences, i.e., $\tau_{\mathrm{Ar}_{3\mathrm{p}}} - \tau_{\mathrm{Ne}_{2\mathrm{p}}}$ and $\tau_{\mathrm{Ar}_{3\mathrm{p}}} - \tau_{\mathrm{He}_{1\mathrm{s}}}$ are listed in table 2, for the sideband order SB58. The delays between photoelectron wavepackets of the electron emitted from the 3p shell of Ar and 2p shell of Ne, and the 3p shell of Ar and the 1s shell of He, as extracted from the fit results are 15.8 ± 3.4 as averaged over 11 scans and 7.9 ± 1.5 as averaged over 9 scans, respectively.

For a many-electron atom, the delay contains information about the contributions from different photoionization channels and their coupling (inter-shell correlation) which can be accounted for in the the random-phase approximation with exchange (RPAE). This theoretical method

Table 1. **Calculated Wigner time delays τ_W (obtained using RPAE method [47]) and continuum-continuum corrections τ_{CC} at 90 eV. The delays for low photon energies of 31 eV, 34.1 eV and 37.2 eV obtained from [39] are shown for comparison. All delays τ are given in attoseconds.**

$E_{h\nu}$ / eV	Ne_{2p}			Ar_{3p}			He_{1s}		
	τ_{cc}	τ_{cc+W}	τ_W	τ_{cc}	τ_{cc+W}	τ_W	τ_{cc}	τ_{cc+W}	τ_W
90.0	-7.8	-3.9	3.8	-7.0	-7.8	-0.8	-8.2	-7.0	0.7
37.2	-45.5	-23.8	21.7	-31.6	-0.2	31.4	-56.3	-56.3	-0.0
34.1	-59.0	-29.9	29.1	-38.0	12.6	50.6	77.1	-47.4	-29.7
31.0	-82.0	-37.9	44.1	-47.0	8.9	55.9	-120.0	-62.5	57.5

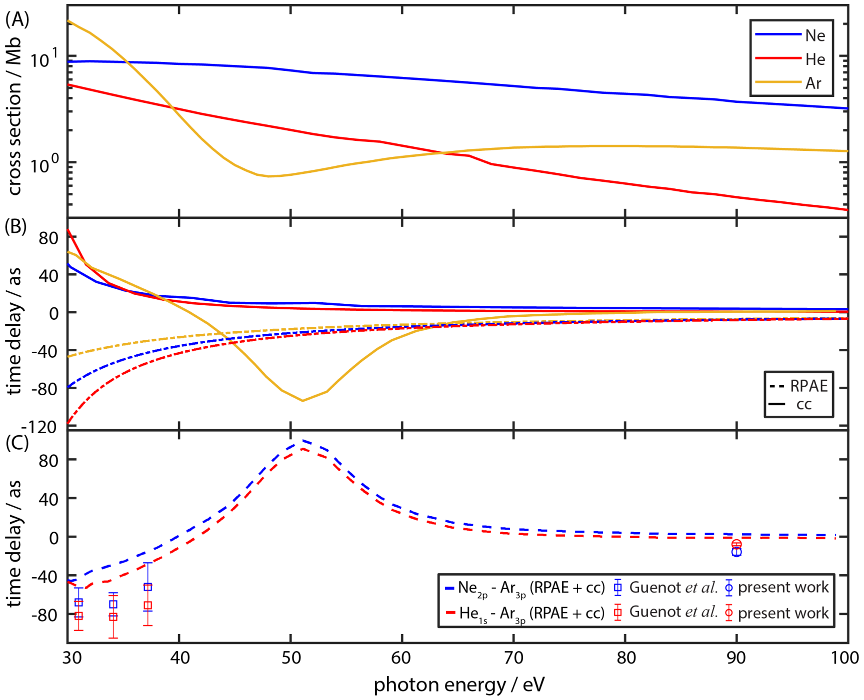

Fig. 7. Calculated and experimental photoionization parameters. (A) Energy dependent photoemission cross sections for Ne, He and Ar (B) RPAE calculations for the Wigner time delay [45] (solid lines) and continuum-continuum correction [15] (dashed lines) (C) The relative theoretical RPAE delays including τ_{CC} for $Ne_{2p} - Ar_{3p}$ (blue) and $He_{1s} - Ar_{3p}$ (red). The measured relative delays at 90 eV photon energy with the respective error bars (red and blue circles) are shown for comparison. The measured relative delays for low photon energies of 31 eV, 34.1 eV and 37.2 eV (read and blue squares) obtained from [39] are shown for comparison.

represents the state-of-the-art in atomic photoionization and takes both independent-electron and inter-shell correlation effects into account.

Figure 7(A) presents the cross section for the dominant channels in the photoionization of Ne, Ar and He [47]. The τ_W and τ_{CC} over a broad energy range are shown in Fig. 7(B). The atomic delays excluding the τ_{CC} have been obtained using the RPAE model, where the inter-shell electron correlations are included, as opposed to the Hartree-Fock (HF) method which is shown for comparison in Ref. [47]. Here, the delays from the outer-valence shell of neon corresponds to

2p→Es/d, argon to 3p→Es/d and for helium to 1s→Ep. Due to absence of any resonances in the investigated energy range, the multi-configuration Hartree-Fock (MCHF) model is not required. The experimental results $\Delta\tau_{\mathrm{meas}}$ in Tab. 2 are compared to the theoretical $\tau_{\mathrm{W}} + \tau_{\mathrm{CC}}$ in Fig. 7(C).

Table 2. **Measured delays $\Delta\tau_{\mathrm{meas}}$ versus calculated difference $\Delta\tau_{\mathrm{calc}} = \tau_{\mathrm{CC+W_1}} - \tau_{\mathrm{CC+W_2}}$ of the Wigner time delays τ_{W} [47] and continuum-continuum corrections τ_{CC}. The delays for low photon energies of 31 eV, 34.1 eV and 37.2 eV obtained from [39] are shown for comparison. All delays τ are given in attoseconds.**

$\mathrm{gas}_{\mathrm{shell}}$	$E_{h\nu}$	$\Delta\tau_{\mathrm{meas}}$	$\tau_{\mathrm{cc+W_1}}$	$\tau_{\mathrm{cc+W_2}}$	$\Delta\tau_{\mathrm{calc}}$
$\mathrm{Ar_{3p} - Ne_{2p}}$	90.0	15.8 ± 3.4	−7.8	−3.9	−3.9
	37.2	52 ± 25	−0.2	−23.8	23.6
	34.1	70 ± 12	8.0	−29.9	38.0
	31.0	68 ± 15	8.9	−37.9	46.8
$\mathrm{Ar_{3p} - He_{1s}}$	90.0	7.9 ± 1.5	−7.8	−7.5	−0.3
	37.2	52 ± 25	−0.2	−38.0	37.8
	34.1	70 ± 12	8.0	−47.4	55.0
	31.0	68 ± 15	8.9	−62.5	71.4

The atom-independent continuum-continuum delays for different kinetic energies of an electron, as calculated from [15], are shown in Fig. 8, where the contribution for Ar, He and Ne for photon energies of $E_{h\nu} = 35\,\mathrm{eV}$ (red) and $E_{h\nu} = 90\,\mathrm{eV}$ (blue) are highlighted. As the photoelectron kinetic energy increases, the τ_{CC} delays play a minor role as the delay difference between different gases decrease to much smaller values, as seen in Table 1 and in Fig. 8. Whereas for the measurements done by Guénot *et al.* [39] at low photon energies, the continuum-continuum delay differences $\Delta\tau_{\mathrm{CC}}$ are on the order of 15 to 70 as and account for a major fraction of the observed delay difference, this is not the case for our measurements at much higher photon energies of 90 eV, where the differences from $\Delta\tau_{\mathrm{CC}}$ reduce to 1 to 1.5 as and are an insignificant fraction of the measured total delays $\Delta\tau_{\mathrm{meas}}$. Moving to higher photon energies, and benchmarking with gas mixtures further provides the advantage that the τ_{CC} delay differences are negligible at high photon energies. This is not a trivial distinction. This implies that these measurements can be used to pin down the contributions arising exclusively from differences in the Wigner photoionization delays. The agreement between the experiment and theory is reasonable and within 10 as of the theoretical predictions [47] used. As compared to the state-of-the-art RABBITT measurements demonstrated earlier using only filters with significant error margins [39], our technique results in a much higher accuracy (cf. Table 2) as it decreases the spectral complexity. Due to the reasons discussed before, RABBITT has not been demonstrated at such high photon energies for gas mixtures. We have presented the first experiment reporting such measurements. We have found a single reference reporting theoretical calculations at high photon energies [47]. The RPAE theory does not take into account the IR probing field as it is designed for continuous XUV field synchrotron measurements only. Conversely, the TDSE calculation [49] takes into account both the XUV and IR fields but it does not recognize the inter-shell correlation. Neither of them is incomplete and the difference with the experiment may indicate the need to develop a theory which takes into account the inter-shell correlation and the XUV/IR fields simultaneously. Such a complete theory is yet to be developed. We believe that more accurate calculations are needed to explain the present results, which is beyond the scope of the present work. Our proposed experimental scheme and results will enable and trigger more measurements and also further development of theory, where the subtle differences, only highlighted at high photon energies can no longer be overlooked.

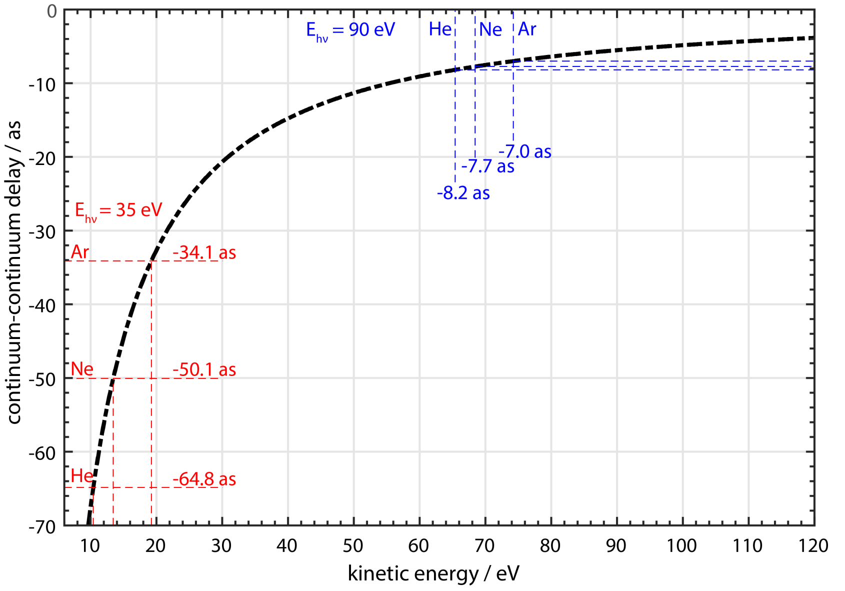

Fig. 8. Calculated continuum-continuum (cc) delays. CC delays calculated from the phase shifts for stimulated emission of one laser photon of 800 nm laser photon, in a Coulomb potential with $Z = 1$ for different kinetic energies of the emitted photoelectron. Ar, He and Ne τ_{CC} are highlighted for photon energies of $E_{h\nu} = 35$ eV (red) and $E_{h\nu} = 90$ eV (blue).

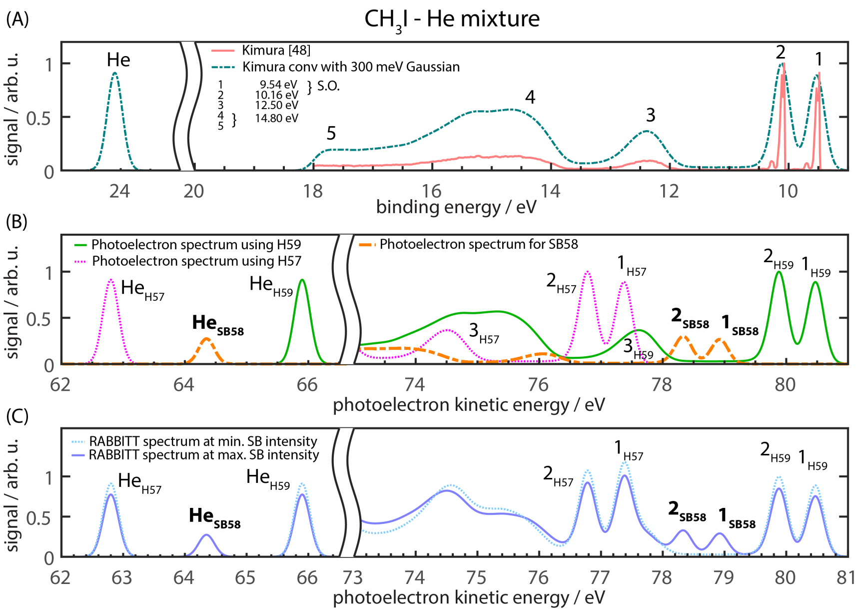

Fig. 9. Simulated photoelectron spectra for CH$_3$I-He mixture. (A) Photoelectron spectrum on the binding energy of CH$_3$I measured with a narrowband source (Kimura *et al.* [50]) and convoluted with our spectrometer resolution of 300 meV. A photoelectron peak at 24.6 eV with a 300 meV width is shown for helium. (B) Individual photoelectron contribution from H57, H59 and SB58 on the photoelectron kinetic energy axis. (C) Projection of RABBITT trace for delay positions of minimum (dotted) and maximum (line) SB intensity.

5. Molecule - gas mixture

Here, we demonstrate that our scheme is not restricted to rare gases but will also find applications in molecules. We use a molecule-gas mixture of CH_3I and He and simulate the expected photoelectron spectra. Fig. 9(A) shows the photoelectron spectra on the binding energy axis for CH_3I for a narrowband source [50] and convoluted with a 300 meV Gaussian, corresponding to the bandwidth of our individual harmonic lines and spectral resolution of the TOF detector. In addition, a photoelectron peak at 24.6 eV with a 300 meV width is shown for helium. The ratio between CH_3I and the He peak is chosen arbitrarily as it can be experimentally chosen by changing the ratio of the gas mixture. In the presence of two harmonics, H57 (pink) and H59 (green), which is the case for our experiment, their individual photoelectron contributions are compared with those of SB58 on the photoelectron kinetic energy axis in Fig. 9(B). This is then used to obtain the projection of the interferogram trace (RABBITT) at position of maximum sideband intensity (violet) and minimum sideband intensity (blue-dotted) in Fig. 9(C), clearly demonstrating the experimental advantage of our scheme. This can be used to benchmark the delays in CH_3I and other molecules to theoretically well investigated helium.

6. Summary and outlook

We have presented our experimental setup which allows for the selection of two odd harmonic orders. This overcomes the limitations that so far prevented RABBITT measurements at high photon energies. We demonstrate the application of this scheme by measurements of photoemission time-delays between different atomic gases. Existing theoretical models need to be further improved as high energies provide a unique region with little or no contributions from the τ_{CC} delays. This can be used to study the difference in photoionization time delays between different species. We also show that our scheme is not limited to just rare gases and can easily be extended to molecules, liquids and solids.

A systematic study at different energies for different target gases can be performed. Using the field-free TOF geometry as shown, angle-resolved RABBITT measurements can be performed by changing the input polarization using a $\lambda/2$-waveplate. The experimental setup can be further used for comparing delays from attosecond streaking and RABBITT measurements under the same experimental conditions.

By enabling RABBITT measurements at photon energies where previously only streaking was possible, our work further opens the following new possibilities (a) performing time-delay measurements with high spectral resolution that distinguish photoelectrons from shake-up bands [19], and also resolve Auger lines and other satellite bands (b) enabling time-delay measurements in energy regions free of resonances (c) measuring delays between more than two orbitals in both atoms and molecules (d) probing electron-correlation effects by accessing inner-valence orbitals of atoms and molecules, which have stronger electron correlation than valence orbitals. Our scheme is not just limited to measurement of photoionization time delays, but can also be used to measure Auger decay, laser-induced Auger decay and other types of electronic dynamics triggered by inner-valence of core-level ionization.

Funding

ERC Starting Grant (contract 307270-ATTOSCOPE), ETH Zürich and SNF grant no. 200021E-162822.

Acknowledgment

A.J. and T.G. contributed equally to this work. The authors would like to acknowledge the support of Andreas Schneider, Andrés Laso and Markus Kerellaj from ETH LPC electronics and mechanical workshop. The authors also thank Shutaro Karashima for support during the experiment, Martin Huppert for fruitful discussions on the harmonic source and Inga Jordan for discussions on the complex fit method.